

1 **Tropopause Evolution in a Rapidly Intensifying Tropical Cyclone: A Static**
2 **Stability Budget Analysis in an Idealized, Axisymmetric Framework**

3 Patrick Duran* and John Molinari

4 *University at Albany, State University of New York, Albany, NY*

5 **Corresponding author address:* Department of Atmospheric and Environmental Sciences, Univer-
6 sity at Albany, State University of New York, 1400 Washington Avenue, Albany, NY.

7 E-mail: pduran2008@gmail.com

ABSTRACT

8 Large changes in tropopause-layer static stability are examined during the
9 rapid intensification (RI) of a tropical cyclone (TC) in an idealized, axisym-
10 metric simulation. Over the eye, static stability near the tropopause decreases
11 and the cold-point tropopause height rises by up to 4 km at the storm center.
12 Outside of the eye, static stability increases considerably just above the cold-
13 point tropopause, and the tropopause remains near its initial level.

14 A budget analysis reveals that the advection term, which includes differen-
15 tial advection of potential temperature and direct advection of static stability,
16 is important throughout the upper troposphere and lower stratosphere. Within
17 the eye, differential advection plays a particularly important role in destabi-
18 lizing the layer near and above the cold-point tropopause. Outside of the eye,
19 the upper-tropospheric outflow layer exports high potential temperature (θ)
20 air from the eyewall to large radii in the upper troposphere. This increase in
21 θ forces stabilization below the outflow jet and destabilization above. Vertical
22 wind shear above and below the outflow maximum induces vertical gradi-
23 ents of turbulence, which also modify the vertical stability profile. Mean-
24 while, radiative cooling tendencies at the top of the cirrus canopy generally
25 act to destabilize the upper troposphere and stabilize the lower stratosphere.
26 These turbulent and radiative processes combine to play an important role in
27 the development of the strong stable layer immediately above the cold-point
28 tropopause during RI.

29 **1. Introduction**

30 Using a high-resolution dropsonde dataset collected during the Tropical Cyclone Intensity Ex-
31 periment (TCI; Doyle et al. 2017), Duran and Molinari (2018) observed dramatic changes in
32 tropopause structure during the rapid intensification (RI) of Hurricane Patricia (2015). The goal of
33 the present paper is to analyze the processes that might have produced the upper-tropospheric and
34 lower-stratospheric fluctuations observed in Patricia using an idealized axisymmetric simulation.

35 After undergoing a remarkably rapid intensification (RI), Hurricane Patricia (2015) attained the
36 strongest wind speed ever recorded in a tropical cyclone (TC) (Kimberlain et al. 2016; Rogers et al.
37 2017). TCI dropsonde observations collected during this RI period revealed dramatic changes in
38 the cold-point tropopause height and upper-level static stability (Duran and Molinari 2018). In
39 particular, when Patricia was at tropical storm intensity shortly before RI commenced, a strong
40 inversion layer existed just above the cold-point tropopause (see their Fig. 4a). During the first
41 half of the RI period, this inversion layer weakened throughout Patricia’s inner core, with the
42 weakening most pronounced over the developing eye. By the time the storm reached its maximum
43 best-track intensity of 95 m s^{-1} , the inversion layer over the eye had disappeared almost completely
44 (see their Fig. 4d), which was accompanied by a greater than 1-km increase in the tropopause
45 height. Meanwhile outside of the eye, the static stability remained large and the tropopause stayed
46 near its initial level.

47 Despite the importance of tropopause-layer thermodynamics in theoretical models of hurri-
48 canes (Emanuel and Rotunno 2011; Emanuel 2012), most observational studies of the upper-
49 tropospheric structure of TCs are decades old¹. Recently, however, Komaromi and Doyle (2017)
50 found that stronger TCs tended to have a higher and warmer tropopause over their inner core than
51 weaker TCs. Their results are consistent with the evolution observed over the inner core of Hur-

¹ An in-depth review of these papers can be found in Duran and Molinari (2018).

52 ricane Patricia, in which the tropopause height increased and the tropopause temperature warmed
53 throughout RI (Duran and Molinari 2018).

54 An idealized simulation of a TC analyzed by Ohno and Satoh (2015) suggested that the devel-
55 opment of an upper-level warm core near the 13-km level acted to decrease the static stability near
56 the tropopause within the eye. During the early stage of development in their simulation, large
57 static stability existed above 16 km at all radii (their Fig. 9c). However, after the storm's inten-
58 sification, the static stability within the eye above 16 km was markedly smaller (their Fig. 10c).
59 Although the mechanisms that might drive this static stability evolution have not been examined
60 explicitly, it might be related to the development of an upper-tropospheric warm core within the
61 eye.

62 Stern and Zhang (2013) described the development of the TC warm core using a potential tem-
63 perature (θ) budget analysis. Although the warm anomaly in their simulation maximized in the
64 mid-levels, they noted that a secondary warming maximum also existed in the 12-14-km layer.
65 Radial and vertical advection both played important roles in this warm core development through-
66 out RI, and subgrid-scale diffusion became particularly important during the later stage of RI.
67 The warming of the upper troposphere by these advective and diffusive processes could decrease
68 the vertical θ gradient, thereby contributing to a decrease in static stability near the tropopause
69 within the eye.

70 Outside of the eye, in the presence of cirrus clouds, vertical gradients of radiative heating also
71 can modify the tropopause-layer static stability. Bu et al. (2014) noted the existence of a shallow
72 region of diurnal-mean net radiative cooling at the top of the TC cirrus canopy (see their Figs. 5,
73 11). This shallow region of cooling could act to destabilize the layer just below the top of the cirrus
74 canopy and stabilize the layer immediately above. If the top of the cirrus canopy lies close to the
75 tropopause, these radiative processes could contribute to a stabilization of the lower stratosphere.

76 To our knowledge, the only paper that has examined explicitly the static stability evolution
77 in a modeled TC is Kepert et al. (2016), but their analysis was limited to the boundary layer.
78 The analysis herein is based upon that of Stern and Zhang (2013), except using a static stability
79 budget similar to that of Kepert et al. (2016), with a focus on the upper-tropospheric and lower-
80 stratospheric evolution during RI.

81 **2. Model Setup**

82 The numerical simulations were performed using version 19.4 of Cloud Model 1 (CM1) de-
83 scribed in Bryan and Rotunno (2009). The equations of motion were integrated on a 3000-km-
84 wide, 30-km-deep axisymmetric grid with 1-km horizontal and 250-m vertical grid spacing. The
85 computations were performed on an f -plane at 15°N latitude, over a sea surface with constant
86 temperature of 30.5°C, which is based on that analyzed near Hurricane Patricia (2015; Kimberlain
87 et al. 2016). Horizontal turbulence was parameterized using the Smagorinsky scheme described
88 in Bryan and Rotunno (2009, pg. 1773), with a prescribed mixing length that varied linearly from
89 100 m at a surface pressure of 1015 hPa to 1000 m at a surface pressure of 900 hPa. Vertical
90 turbulence was parameterized using the formulation of Markowski and Bryan (2016, their Eq.
91 6), using an asymptotic vertical mixing length of 100 m, which is the default setup for hurricane
92 simulations in CM1. A Rayleigh damping layer was applied outside of the 2900-km radius and
93 above the 25-km level to prevent spurious gravity wave reflection at the model boundaries. Mi-
94 crophysical processes were parameterized using the Thompson et al. (2004) scheme, and radiative
95 heating tendencies were computed every two minutes using the Rapid Radiative Transfer Model
96 for GCMs (RRTMG) longwave and shortwave schemes (Iacono et al. 2008). The initial temper-
97 ature and humidity field was horizontally homogeneous and determined by averaging all Climate
98 Forecast System Reanalysis (CFSR) grid points within 100 km of Patricia’s center of circulation

at 18 UTC 21 October 2015. The vortex described in Rotunno and Emanuel (1987, their Eq. 37) was used to initialize the wind field, setting all parameters equal to the values used therein.

Although hurricanes simulated in an axisymmetric framework tend to be more intense than those observed in nature, the intensity evolution of this simulation matches reasonably well with that observed in Hurricane Patricia. After an initial spin-up period of about 20 hours, the modeled storm (Fig. 1, blue lines) began an RI period that lasted approximately 18 hours. After this RI, the storm continued to intensify more slowly until the maximum 10-m wind speed reached 89 m s^{-1} and the sea-level pressure reached its minimum of 846 hPa 81 hours into the simulation. Hurricane Patricia (red stars) exhibited a similar intensity evolution prior to its landfall, with an RI period leading to a maximum 10-m wind speed of 95 m s^{-1} and a minimum sea-level pressure of 872 hPa.

3. Budget Computation

Following Bryan (2017), the static stability can be expressed as the squared Brunt-Väisälä frequency:

$$N_m^2 = \frac{g}{T} \left(\frac{\partial T}{\partial z} + \Gamma_m \right) \left(1 + \frac{T}{R_d/R_v + q_s} \frac{\partial q_s}{\partial T} \right) - \frac{g}{1 + q_t} \frac{\partial q_t}{\partial z}, \quad (1)$$

where g is gravitational acceleration, T is temperature, R_d and R_v are the gas constants of dry air and water vapor, respectively, q_s is the saturation mixing ratio, q_t is the total condensate mixing ratio, and Γ_m is the moist-adiabatic lapse rate:

$$\Gamma_m = g(1 + q_t) \left(\frac{1 + L_v q_s / R_d T}{c_{pm} + L_v \partial q_s / \partial T} \right), \quad (2)$$

where L_v is the latent heat of vaporization and c_{pm} is the specific heat of moist air at constant pressure. In the tropopause layer, q_s , q_t , $\partial q_s / \partial T$, and $\partial q_t / \partial z$ approach zero. In this limiting case, Eq. 1 reduces to:

$$N^2 = \frac{g}{\theta} \frac{\partial \theta}{\partial z}, \quad (3)$$

118 where θ is the potential temperature.

119 Eq. 1 is the appropriate expression for N^2 in moist environments, whereas Eq. 3 applies strictly
 120 in the absence of moisture. Although the tropopause layer is not completely dry, moisture is small
 121 enough there for Eq. 3 to be a good approximation of N^2 in the the budget computation².

122 Taking the time derivative of Eq. 3 and switching the order of differentiation yields the static
 123 stability tendency:

$$\frac{\partial N^2}{\partial t} = \frac{g}{\theta} \frac{\partial}{\partial z} \frac{\partial \theta}{\partial t} - \frac{g}{\theta^2} \frac{\partial \theta}{\partial z} \frac{\partial \theta}{\partial t}, \quad (4)$$

124 where the potential temperature tendency, $\partial \theta / \partial t$, can be written, following Bryan (2017):

$$\frac{\partial \theta}{\partial t} = -u \frac{\partial \theta}{\partial r} - w \frac{\partial \theta}{\partial z} + HTURB + VTURB + MP + RAD + DISS \quad (5)$$

125 Each term on the right-hand side of Eq. 5 represents a θ budget variable, each of which is output
 126 directly by the model every minute.

127 The first term on the right-hand side of Eq. 4 is larger than the second term throughout most of
 128 the tropopause layer (not shown). Consequently, the contribution of each of the terms in Eq. 5 to
 129 the N^2 tendency can be interpreted in terms of a vertical gradient of each term.

130 Taking the vertical gradient of the first two terms on the right-hand side of Eq. 5 yields the time
 131 tendency of the vertical θ gradient due to horizontal and vertical advection:

$$\left(\frac{\partial}{\partial t} \frac{\partial \theta}{\partial z} \right)_{adv} = -u \frac{\partial}{\partial r} \frac{\partial \theta}{\partial z} - w \frac{\partial}{\partial z} \frac{\partial \theta}{\partial z} - \frac{\partial u}{\partial z} \frac{\partial \theta}{\partial r} - \frac{\partial w}{\partial z} \frac{\partial \theta}{\partial z}. \quad (6)$$

132 The first two terms on the right-hand side of Eq. 6 represent advection of static stability by the
 133 radial and vertical wind, respectively. These terms act to rearrange the static stability field, but
 134 cannot strengthen or weaken static stability maxima or minima. The third and fourth terms on
 135 the right-hand side of Eq. 6 represent, respectively, the tilting of isentropes in the presence of

²The validity of this approximation will be substantiated later in this section.

vertical wind shear, and the stretching or squashing of isentropes by vertical gradients of vertical velocity. Since these terms involve velocity gradients, they can act to strengthen or weaken static stability maxima or minima through differential advection. Unless otherwise stated, any reference to “advection” in this paper indicates the sum of all of the terms in Eq. 6.

Returning to Eq. 5, HTURB and VTURB are the θ tendencies from the horizontal and vertical turbulence parameterizations, MP is the tendency from the microphysics scheme, RAD is the tendency from the radiation scheme, and DISS is the tendency due to turbulent dissipation. This equation neglects Rayleigh damping, since the entire analysis domain lies outside of the regions where damping is applied. Each term in Eq. 5 is substituted for $\partial\theta/\partial t$ in Eq. 4, yielding the contribution of each budget term to the static stability tendency. These terms are summed, yielding an instantaneous “budget change” in N^2 every minute. The budget changes are then averaged over 24-hour (1440-minute) periods, multiplied by the length of the time period, and compared to the total model change in N^2 over that same time period, i.e.:

$$\Delta N_{budget}^2 = \frac{\delta t}{1440} \sum_{t=t_0}^{1440} \left. \frac{\partial N^2}{\partial t} \right|_t \quad (7)$$

$$\Delta N_{model}^2 = N_{t_0+\delta t}^2 - N_{t_0}^2 \quad (8)$$

$$Residual = \Delta N_{model}^2 - \Delta N_{budget}^2 \quad (9)$$

where t_0 is an initial time and δt is 24 hours.

Eqs. 7-9 are evaluated for three consecutive 24-hour periods in Fig. 2. For this and all subsequent radial-vertical cross sections, a 1-2-1 smoother is applied once in the radial direction to eliminate $2\Delta r$ noise that appears in some of the raw model output and calculated fields. The left column of Fig. 2 depicts the model changes computed using Eq. 8, together with Eq. 1 in saturated environments and Eq. 3 in subsaturated environments. The center column depicts the budget changes computed using Eq. 7 together with Eq. 4 throughout the entire domain. Thus, the left

column includes the effect of moisture in the N^2 computations, whereas the center column neglects moisture. The right column depicts the residuals, computed using Eq. 9 (i.e. the left column minus the center column.) In every 24-hour period, the budget changes are nearly identical to the model changes, which is reflected in the near-zero residuals in the right column. This indicates that the budget accurately represents the model variability, which implies that the neglect of moisture in the budget computation introduces negligible error within the analysis domain³.

In the tropopause layer, some of the budget terms are small enough to be ignored. To determine which of the budget terms are most important, a time series of the contribution of each of the budget terms in Eq. 5 to the tropopause-layer static stability tendency is plotted in Fig. 3. For this figure, each of the budget terms is computed using the method described in Section 3, except with 1-hour averaging intervals instead of 24-hour intervals. The absolute values of these tendencies are then averaged over the radius-height domain of the plots shown in Fig. 2 and plotted as a time series⁴. Advection (Fig. 3, red line) plays an important role in the mean tropopause-layer static stability tendency at all times, and vertical turbulence (Fig. 3, blue line) and radiation (Fig. 3, dark green line) also contribute significantly. The remaining three processes - horizontal turbulence, microphysics, and dissipative heating - are negligible everywhere outside of the eyewall, and do not play important roles in the mesoscale tropopause variability.

The preceding analysis indicates that, at all times, three budget terms dominate the tropopause-layer static stability tendency: advection, vertical turbulence, and radiation. Variations in the

³This is not the case in the lower- and mid-troposphere, where the residual actually exceeds the budget tendencies in many places, likely due to the neglect of moisture; thus we limit this analysis to the upper troposphere and lower stratosphere.

⁴It will be seen in subsequent figures that each of the terms contributes both positively and negatively to the N^2 tendency within the analysis domain. Thus, taking an average over the domain tends to wash out the positive and negative contributions. To circumvent this problem, the absolute value of each of the terms is averaged.

177 magnitude and spatial structure of these terms drive the static stability changes depicted in Fig. 2;
178 subsequent sections will focus on these variations and what causes them.

179 **4. Results**

180 *a. Static stability and tropopause evolution*

181 The average N^2 over the first day of the simulation (Fig. 4a) indicates the presence of a weak
182 N^2 maximum just above the cold-point tropopause. Over the subsequent 24 hours, during the
183 RI period, the N^2 maximum weakened within the 25-km radius (Fig. 4b). This decreasing N^2
184 corresponded to an increase in the tropopause height within the developing eye, maximized at the
185 storm center. Outside of the eye, meanwhile, the tropopause height decreased over the eyewall
186 region (25-60-km radius) and increased only slightly outside of the 60-km radius. In this outer
187 region, the N^2 maximum just above the tropopause strengthened during RI. These trends continued
188 as the storm's intensity leveled off in the 48-72-hour period (Fig. 4c). The tropopause height
189 increased to nearly 21 km at the storm center and sloped sharply downward to 16.3 km on the inner
190 edge of the eyewall, near the 30 km radius. A local minimum in tropopause height manifested near
191 the eye-eyewall interface, similar to that observed in Hurricane Patricia (see Duran and Molinari
192 2018, Figs. 4f-h), although the authors of that paper cautioned that these local minima could
193 be quite sensitive to small fluctuations in temperature. The presence of a local minimum at this
194 location in these 24-hour averages, however, suggests that this tropopause depression on the outer
195 edge of the eye could be a robust, persistent feature. Static stability outside of the eye, meanwhile,
196 continued to increase just above the cold-point tropopause. This N^2 evolution closely follows that
197 observed in Hurricane Patricia (2015; Duran and Molinari 2018, see their Fig. 4). The mechanisms
198 that led to these N^2 changes will be investigated in the subsequent sections.

199 *b. Static stability budget analysis*

200 *(i) 0-24 hours*

201 The initial spin-up period was characterized by a steady increase of the maximum wind speed
202 from 11 m s^{-1} to 22 m s^{-1} (Fig. 1a, blue line), an intensification rate that closely matched that of
203 TC Patricia (Fig. 1a, red stars). The weakening of the lower-stratospheric static stability maximum
204 during this period is reflected in the total N^2 budget change over this time (Fig. 5a). The layer just
205 above the cold-point tropopause was characterized by decreasing N^2 (purple shading), maximizing
206 at the storm center. At and immediately below the tropopause, meanwhile, N^2 increased during
207 this time period (green shading). Although these tendencies extended out to the 200-km radius,
208 they were particularly pronounced at innermost radii. A comparison of the contributions of advec-
209 tion (Fig. 5b), vertical turbulence (Fig. 5c), and radiation (Fig. 5d) reveals that advection was the
210 primary driver of the N^2 tendency during this period, acting to stabilize near and just below the
211 tropopause and destabilize above. Although vertical turbulence acted in opposition to advection
212 (i.e. it acted to stabilize regions that advection acted to destabilize), the magnitude of the advec-
213 tive tendencies was larger, particularly at the innermost radii. The sum of advection and vertical
214 turbulence (Fig. 5e) almost exactly replicated the static stability tendencies above the tropopause.
215 Radiative tendencies, meanwhile, (Fig. 5d) acted to destabilize the layer below about 16 km and
216 stabilize the layer between 16 and 17 km. The sum of advection, vertical turbulence, and radiation
217 (Fig. 5f) reproduced the total change in N^2 almost exactly.

218 *(ii) 24-48 hours*

219 During the RI period, the maximum wind speed increased from 22 m s^{-1} to 80 m s^{-1} (Fig. 1a).
220 Over this time, N^2 within the eye generally decreased above 16 km and increased below (Fig. 6a),
221 with the destabilization above 16 km maximizing near the level of the mean cold-point tropopause.

222 These tendencies at the innermost radii were driven almost entirely by advection (Fig. 6b). Vertical
223 turbulence (Fig. 6c) and radiation (Fig. 6d) contributed negligibly to the static stability tendencies
224 in this region.

225 Outside of the eye, the N^2 evolution exhibited alternating layers of positive and negative tenden-
226 cies. Near and above 18 km existed an upward-sloping region of decreasing N^2 that extended out
227 to the 180-km radius. In this region, neither vertical turbulence nor radiation exhibited negative N^2
228 tendencies; advection was the only forcing for this destabilization. Immediately below this layer,
229 just above the cold-point tropopause, was a region of increasing N^2 that sloped upward from 17
230 km near the 30-km radius to just below 18 km outside of the 100-km radius. Advection and verti-
231 cal turbulence both contributed to this positive N^2 tendency, with advection playing an important
232 role below about 17.5 km and and turbulence playing an important role above. The sum of advec-
233 tion and turbulence (Fig. 6e) reveals two separate regions of increasing N^2 in the 17-18-km layer
234 rather than one contiguous region. The addition of radiation to these two terms, however, (Fig. 6f)
235 provides the link between these two regions, indicating that radiation also plays a role in strength-
236 ening the stable layer just above the tropopause. In the 16-17-km layer, just below the cold-point
237 tropopause, a horizontally-extensive layer of destabilization also was forced by a combination of
238 advection, vertical turbulence, and radiation. The sum of advection and vertical turbulence ac-
239 counts for only a portion of the decreasing N^2 in this layer, and actually indicates forcing for
240 stabilization near the 50-km radius and outside of the 130-km radius. Radiative tendencies over-
241 come this forcing for stabilization in both of these regions to produce the radially-extensive region
242 of destabilization observed just below the tropopause.

243 The sum of advection, vertical turbulence, and radiation (Fig. 6f) once again closely follows
244 the observed N^2 variability, except in the eyewall region, where the neglect of latent heating and
245 horizontal turbulence introduces some differences.

246 (iii) 48-72 hours

247 After the storm's maximum wind speed leveled off near 80 m s^{-1} (Fig. 1a), the magnitude of
248 the static stability tendencies within the eye decreased to near zero (Fig. 7a). Outside of the eye,
249 however, N^2 continued to decrease in the layer immediately surrounding the tropopause and in-
250 crease just above. The sum of advection and vertical turbulence (Fig. 7e) indicates that these two
251 processes account for most of the destabilization near the tropopause and some of the stabilization
252 near the 18-km altitude. Below the tropopause, however, these two terms provided strong forc-
253 ing for stabilization that was not observed in the budget change (Fig. 7a). Radiation (Fig. 7d),
254 which generally forced stabilization above 17 km and destabilization below, balanced out this
255 forcing for stabilization in the upper troposphere. Within the 30-80-km radial band, advection and
256 vertical turbulence combined to force destabilization in the 17-18-km layer (Fig. 7e), which was
257 not observed in the budget change (Fig. 7a). Radiation provided strong forcing for stabilization,
258 which outweighed this effect and produced net stabilization in a portion of this region. Outside of
259 the 80-km radius, both advection (Fig. 7b) and vertical turbulence (Fig. 7c) provided forcing for
260 stabilization near and just above the 18-km level. The sum of the two terms (Fig. 7e) indicates
261 increasing N^2 near the 18-km level everywhere outside of the 80-km radius, but this stabilization
262 is slightly weaker in the 90-120-km radial band than the observed value. The addition of radiation
263 (Fig. 7f) provided the extra forcing for stabilization required to account for the observed increase
264 in N^2 . Outside of the 120-km radius, the region of radiative forcing for stabilization sloped down-
265 ward, and the increase in N^2 observed near 18 km can be explained entirely by a combination of
266 advection and vertical turbulence.

5. Discussion

a. The role of advection

Advection played an important role in the tropopause-layer N^2 evolution at all stages of intensification, but for brevity, this section will focus only on the RI (24-48-hour) period. To investigate the advective processes more closely, the individual contributions of horizontal and vertical advection during the RI period are shown in Fig. 8, along with the corresponding time-mean radial and vertical velocities and θ . The N^2 tendencies due to the two advective components (Fig. 8a,b) exhibited strong cancellation, consistent with flow that was nearly isentropic. There existed, however, a large region near the tropopause in which the total advective tendency was nonzero (Fig. 6b). These nonzero tendencies were related to the development of the TC's secondary circulation as the storm intensified.

During the RI period, strong radial and vertical circulations developed near the tropopause (Fig. 8c,d), which forced high-magnitude N^2 tendencies due to advection (Fig. 8a,b). A layer of strong outflow formed at and below the tropopause during this period, with the outflow maximum (dashed cyan line) curving from the 14-km level at the 50-km radius to just below the 16-km level outside of the 80-km radius (Fig. 8c). Notably, the N^2 tendency due to horizontal advection (Fig. 8a) tended to switch signs at this line, with stabilization below the outflow maximum and destabilization above. This is consistent with the outflow layer carrying air with increasingly large θ from the eyewall to large radii as the storm intensified. This increase in θ maximized near the outflow maximum, which acted to decrease $\partial\theta/\partial z$ above the outflow maximum and increase it below. This mechanism is the same as that discussed in Trier and Sharman (2009), in which vertical wind shear in the outflow layer of a mesoscale convective system modified the upper-tropospheric static stability through differential advection of isentropes.

290 Meanwhile in the lower stratosphere, a thin layer of $2\text{--}4\text{ m s}^{-1}$ inflow developed a few hundred
291 meters above the tropopause, similar to that which was observed in Hurricane Patricia (2015;
292 Duran and Molinari 2018) and in previous modeling studies (e.g. Ohno and Satoh 2015; Kieu et al.
293 2016). Since the isentropes in this layer sloped slightly upward with radius (i.e. $\partial\theta/\partial r < 0$), this
294 inflow acted to import lower θ air from outer radii to inner radii. Since the negative θ tendencies
295 maximized at the level of maximum inflow, the layer below the inflow maximum destabilized and
296 the layer above stabilized (Fig. 8a).

297 Curiously, horizontal advection contributed to the N^2 tendency everywhere within the eye,
298 even though the mean radial velocity there was near zero. Close examination of the model out-
299 put revealed that these tendencies were forced by advective processes associated with inward-
300 propagating waves. Although the radial velocity perturbations induced by these waves averaged
301 out to zero, the advective tendencies forced by the radial velocity perturbations did not. Addition-
302 ally, when these waves reached $r=0$, a dipole of vertical velocity resulted, with ascent above and
303 descent below. For reasons that remain unclear, the regions of ascent were more persistent than the
304 regions of descent, which resulted in the mean ascent observed near $r=0$ above 17 km in Fig. 8d.

305 Vertical advection also played an important role in the tropopause-layer static stability evolution.
306 Within the eye, subsidence dominated below 17 km, while mean ascent existed near the storm
307 center above 17 km. Although the magnitude of the subsidence was larger at lower altitudes,
308 $\partial\theta/\partial z$ was smaller there. Because $\partial\theta/\partial z$ was smaller, the subsidence at lower levels could not
309 accomplish as much warming as the subsidence at higher levels in the eye, consistent with the
310 results of Stern and Zhang (2013). As a result, vertical advection within the eye stabilized the
311 layer below 16 km during RI.

312 Outside of the 27-km radius, ascent dominated the troposphere, while a 1-1.5-km-deep layer
313 of descent existed immediately above the tropopause. These regions of ascent and descent con-

314 verged just above the tropopause; this convergence acted to compact the isentropes in this layer
315 and increase the static stability. Above the lower-stratospheric subsidence maximum, meanwhile,
316 vertical advection decreased N^2 . Below the tropopause, differential vertical advection increased
317 N^2 within the eyewall region and also at larger radii above the vertical velocity maximum at larger
318 radii. Outside of the eyewall and below the vertical velocity maximum, meanwhile, differential
319 vertical advection acted to decrease N^2 .

320 Comparing the N^2 tendencies forced by horizontal (Fig. 8a) and vertical (Fig. 8b) advection
321 to the total advective tendency seen in Fig. 6b reveals that horizontal advective tendencies domi-
322 nated the troposphere, while vertical advective tendencies dominated the layer near and above the
323 tropopause. Thus, tilting of isentropes in the vicinity of the upper-tropospheric outflow maximum
324 appears to be the most important advective process governing the N^2 tendency in the troposphere,
325 whereas convergence of vertical velocity appears to be the most important advective process near
326 the tropopause.

327 *b. The role of radiation*

328 During the initial spin-up period (0-24 hours; Fig. 9a), convection was not deep enough to
329 deposit large quantities of ice near the tropopause and create a persistent cirrus canopy. Due to the
330 lack of ice particles, the radiative heating tendencies during this period (Fig. 9b) were relatively
331 small and confined to the region above a few particularly strong, although transient, convective
332 towers. During RI (24-48 hours), the eyewall updraft strengthened and a radially-extensive cirrus
333 canopy developed near the tropopause (Fig. 9c). The enhanced vertical gradient of ice mixing ratio
334 at the top of the cirrus canopy induced strong diurnal-mean radiative cooling near the tropopause
335 (Fig. 9d). This cooling exceeded 0.6 K h^{-1} (14.4 K day^{-1}) in some places and sloped downward
336 from the lower stratosphere into the upper troposphere, following the top of the cirrus canopy. A

337 small radiative warming maximum also appeared outside of the 140-km radius below this region
338 of cooling. These results broadly agree with those of Bu et al. (2014; see their Fig. 11a), whose
339 CM1 simulations produced a 0.3 K h^{-1} diurnally-averaged radiative cooling at the top of the cirrus
340 canopy and radiative warming within the cloud that maximized near the 200-km radius. This broad
341 region of radiative cooling acted to destabilize the layer below the cooling maximum and stabilize
342 the layer above, which can be seen in Fig. 6d. The small area of net radiative heating outside of
343 the 140-km radius enhanced the destabilization above 16 km in this region and produced a thin
344 layer of stabilization in the 15-16-km layer.

345 After the TC's RI period completed (48-72 hours), strong radiative cooling remained near the
346 tropopause at inner radii (Fig. 9f), sloping downward with the top of the cirrus canopy to below the
347 tropopause at outer radii. Cooling rates exceeded 1 K h^{-1} (24 K day^{-1}) just above the tropopause
348 between the 30- and 70-km radii. This value is more than three times the maximum cooling rate of
349 0.3 K h^{-1} observed by Bu et al. (2014), a difference that is a consequence of their larger vertical grid
350 spacing compared to that used here, along with a contribution from differing radiation schemes.
351 To compare our results to theirs, we ran a simulation identical to that described in Section 2, except
352 using the NASA-Goddard radiation scheme and 625-m vertical grid spacing, to match those of Bu
353 et al. (2014). This simulation produced a maximum 24-hour-average radiative cooling rate of 0.3
354 K h^{-1} , which agrees with that shown in Bu et al. (2014). Another simulation using 625-m vertical
355 grid spacing and RRTMG radiation produced 24-hour-average cooling rates of up to 0.6 K h^{-1} .
356 This suggests that vertical grid spacing smaller than 625 m is necessary to resolve properly the
357 radiative cooling at the top of the cirrus canopy, and that the results can be quite sensitive to the
358 radiation scheme used.

359 Meanwhile below the tropopause, time-mean radiative warming spread from 30- to 160-km
360 radius within the cirrus canopy. The existence of radiative cooling overlying radiative warming in

361 this region led to radiatively-forced destabilization at and below the tropopause, as was observed
362 in Fig. 7d. Beneath the warming layer existed a region of forcing for stabilization, while a much
363 stronger region of forcing for stabilization existed in the lower stratosphere, above the cooling
364 maximum.

365 The results herein suggest that, after the cirrus canopy developed, radiative heating tendencies
366 considerably destabilized the upper troposphere and stabilized the lower stratosphere.

367 *c. The role of turbulent mixing*

368 Fig. 10 depicts the effect of turbulent mixing on the vertical θ profile of an initially stably-
369 stratified layer. At the initial time in this schematic, θ is assumed to increase with height at a
370 constant rate (Fig. 10, left panel). The imposition of turbulence (blue hatching) adjusts the θ
371 profile within the mixed layer toward a constant value equal to the mean value of that layer in
372 the initial state (Fig. 10, right panel). Just above and just below the mixed layer, however, the θ
373 profile remains undisturbed. Consequently, although turbulent mixing acts to decrease $\partial\theta/\partial z$ in
374 the layer in which it is occurring, it actually increases $\partial\theta/\partial z$ just below and just above the layer.
375 Vertical gradients of turbulent mixing like those depicted here are quite important, particularly on
376 the flanks of the upper-tropospheric outflow jet.

377 Two distinct maxima of vertical eddy diffusivity developed in the tropopause layer as the storm
378 intensified (Fig. 11). Comparison of these turbulent regions to the N^2 tendencies in Figs. 6c and
379 7c reveals that the layers in which vertical eddy diffusivity maximized corresponded to layers of
380 destabilization due to vertical turbulence. Just outside of these layers, however, vertical turbulence
381 acted to increase N^2 . The large vertical gradient of vertical eddy diffusivity near the tropopause
382 played an important role in developing the lower-stratospheric stable layer during RI. These results

383 support the hypothesized role of turbulence in setting the outflow-layer θ stratification in Emanuel
384 and Rotunno (2011).

385 6. Conclusions

386 The simulated N^2 evolution shown herein closely matched that observed during the RI of Hur-
387 ricane Patricia (2015). Three N^2 budget terms dominated in the upper troposphere and lower
388 stratosphere: advection, radiation, and vertical turbulence. Advection dominated within the eye,
389 where it provided forcing for destabilization. Radiation and vertical turbulence played particularly
390 important roles in developing the strong N^2 maximum just above the cold-point tropopause during
391 RI.

392 To put the N^2 variability observed near the tropopause into context, Fig. 12 depicts the model
393 change in N^2 over the RI period (hours 24-48) from 0 to 21 km altitude, along with the vertical
394 eddy diffusivity and the radiative heating rate. The largest changes in N^2 occurred in a relatively
395 shallow layer immediately surrounding the tropopause (Fig. 12a). This shallow layer also con-
396 tained the largest diurnally-averaged radiative heating tendencies found anywhere in the domain
397 (Fig. 12c). Values of vertical eddy diffusivity larger than any found outside of the boundary layer
398 also resided in the upper troposphere (Fig. 12b). The results herein suggest that this turbulence
399 not only develops as a response to the presence of small static stability and large vertical wind
400 shear, as discussed by Molinari et al. (2014) and Duran and Molinari (2016), but also can actively
401 increase the static stability in highly localized regions just above and below the mixed layers.

402 Since two of the most important processes contributing to the N^2 variability are parameter-
403 ized, and one (radiation) closely depends on yet another parameterized process (microphysics),
404 the tropopause-layer N^2 variability could be quite sensitive to the assumptions inherent to the pa-
405 rameterizations used. A better understanding of the microphysical characteristics of the TC cirrus

canopy, its interaction with radiation, and outflow-layer turbulence is critical to understanding the tropopause-layer N^2 evolution.

In this paper, all of the variables were averaged over a full diurnal cycle to eliminate the effects of diurnal variability and isolate the overall storm evolution. Diurnal variations in static stability near the tropopause are potentially of interest with respect to the tropical cyclone diurnal cycle, and will be the subject of future work.

Acknowledgments. We are indebted to George Bryan for his continued development and support of Cloud Model 1. We also thank Jeffrey Kepert, Robert Fovell, and Erika Navarro for helpful conversations related to this work. This research was supported by NSF grant AGS-1636799 and Office of Naval Research Grant N000141712110 as a part of the TCI Departmental Research Initiative.

References

- Bryan, G. H., 2017: The governing equations for CM1. [Available online at http://www2.mmm.ucar.edu/people/bryan/cm1/cm1_equations.pdf].
- Bryan, G. H., and R. Rotunno, 2009: The maximum intensity of tropical cyclones in axisymmetric numerical model simulations. *Mon. Wea. Rev.*, **137**, 1770–1789.
- Bu, Y. P., R. G. Fovell, and K. L. Corbosiero, 2014: Influence of cloud-radiative forcing on tropical cyclone structure. *J. Atmos. Sci.*, **71**, 1644–1622.
- Doyle, J. D., and Coauthors, 2017: A view of tropical cyclones from above: The Tropical Cyclone Intensity (TCI) Experiment. *Bull. Amer. Meteor. Soc.*, **98**, 2113–2134.
- Duran, P., and J. Molinari, 2016: Upper-tropospheric low Richardson number in tropical cyclones: Sensitivity to cyclone intensity and the diurnal cycle. *J. Atmos. Sci.*, **73**, 545–554.

428 Duran, P., and J. Molinari, 2018: Dramatic inner-core tropopause variability during the rapid
 429 intensification of Hurricane Patricia (2015). *Mon. Wea. Rev.*, **146**, 119–134.

430 Emanuel, K., 2012: Self-stratification of tropical cyclone outflow. Part II: Implications for storm
 431 intensification. *J. Atmos. Sci.*, **69**, 988–996.

432 Emanuel, K., and R. Rotunno, 2011: Self-stratification of tropical cyclone outflow. Part I: Impli-
 433 cations for storm structure. *J. Atmos. Sci.*, **68**, 2236–2249.

434 Iacono, M. J., J. S. Delamere, E. J. Mlawer, M. W. Shephard, S. A. Clough, and W. D. Collins,
 435 2008: Radiative forcing by long-lived greenhouse gases: Calculations with the AER radiative
 436 transfer models. *J. Geophys. Res.*, **113** (D13103).

437 Kepert, J. D., J. Schwendike, and H. Ramsay, 2016: Why is the tropical cyclone boundary layer
 438 not “well mixed”? *J. Atmos. Sci.*, **73**, 957–973.

439 Kieu, C., V. Tallapragada, D.-L. Zhang, and Z. Moon, 2016: On the development of double warm-
 440 core structures in intense tropical cyclones. *J. Atmos. Sci.*, **73**, 4487–4506.

441 Kimberlain, T. B., E. S. Blake, and J. P. Cangialosi, 2016: Tropical cyclone report: Hurricane
 442 Patricia. National Hurricane Center. [Available online at www.nhc.noaa.gov].

443 Komaromi, W. A., and J. D. Doyle, 2017: Tropical cyclone outflow and warm core structure as
 444 revealed by HS3 dropsonde data. *Mon. Wea. Rev.*, **145**, 1339–1359.

445 Markowski, P. M., and G. H. Bryan, 2016: LES of laminar flow in the PBL: A potential problem
 446 for convective storm simulations. *Mon. Wea. Rev.*, **144**, 1841–1850.

447 Molinari, J., P. Duran, and D. Vollaro, 2014: Low Richardson number in the tropical cyclone
 448 outflow layer. *J. Atmos. Sci.*, **71**, 3164–3179.

449 Ohno, T., and M. Satoh, 2015: On the warm core of a tropical cyclone formed near the tropopause.
450 *J. Atmos. Sci.*, **72**, 551–571.

451 Rogers, R. F., S. Aberson, M. M. Bell, D. J. Cecil, J. D. Doyle, J. Morgerman, L. K. Shay, and
452 C. Velden, 2017: Re-writing the tropical record books: The extraordinary intensification of
453 Hurricane Patricia (2015). *Bull. Amer. Meteor. Soc.*, **98**, 2091–2112.

454 Rotunno, R., and K. A. Emanuel, 1987: An air-sea interaction theory for tropical cyclones. Part II:
455 Evolutionary study using a nonhydrostatic axisymmetric numerical model. *J. Atmos. Sci.*, **44**,
456 542–561.

457 Stern, D. P., and F. Zhang, 2013: How does the eye warm? Part I: A potential temperature budget
458 analysis of an idealized tropical cyclone. *J. Atmos. Sci.*, **70**, 73–89.

459 Thompson, G., R. M. Rasmussen, and K. Manning, 2004: Explicit forecasts of winter precipitation
460 using an improved bulk microphysics scheme. Part I: Description and sensitivity analysis. *Mon.*
461 *Wea. Rev.*, **132**, 519–542.

462 Trier, S. B., and R. D. Sharman, 2009: Convection-permitting simulations of the environment sup-
463 porting widespread turbulence within the upper-level outflow of a mesoscale convective system.
464 *Mon. Wea. Rev.*, **137**, 1972–1990.

LIST OF FIGURES

- Fig. 1.** The maximum 10-m wind speed (top panel; m s^{-1}) and minimum sea-level pressure (bottom panel; hPa) in the simulated storm (blue lines; plotted every minute) and from Hurricane Patricia's best track (red stars; plotted every six hours beginning at the time Patricia attained tropical storm intensity). The rapid weakening during the later stage of Patricia's lifetime was induced by landfall. 25
- Fig. 2.** Left panels: Twenty-four-hour changes in squared Brunt-Väisälä frequency (N^2 ; 10^{-4} s^{-2}) computed using Eq. 8 over (top row) 0-24 hours, (middle row) 24-48 hours, (bottom row) 48-72 hours. Middle Panels: The N^2 change over the same time periods computed using Eqs. 4-7, Right Panels: The budget residual over the same time periods, computed by subtracting the budget change (middle column) from the model change (left column). Orange lines represent the cold-point tropopause height averaged over the same time periods. 26
- Fig. 3.** Time series of the contribution of each of the budget terms to the time tendency of the squared Brunt-Väisälä frequency (N^2 ; 10^{-4} s^{-2}). For each budget term, the absolute value of the N^2 tendency is averaged temporally over 1-hour periods (using output every minute), and spatially in a region extending from 0 to 200 km radius and 14 to 21 km altitude. 27
- Fig. 4.** Twenty-four-hour averages of squared Brunt-Väisälä frequency (N^2 ; 10^{-4} s^{-2}) over (a) 0-24 hours, (b) 24-48 hours, (c) 48-72 hours. Orange lines represent the cold-point tropopause height averaged over the same time periods. 28
- Fig. 5.** (a) Total change in N^2 over the 0-24-hour period ($10^{-4} \text{ s}^{-2} (24 \text{ h})^{-1}$) and the contributions to that change from (b) the sum of horizontal and vertical advection, (c) vertical turbulence, (d) longwave and shortwave radiation, (e) the sum of horizontal advection, vertical advection, and vertical turbulence, and (f) the sum of horizontal advection, vertical advection, vertical turbulence, and longwave and shortwave radiation. Green shading indicates regions of stabilization and purple shading indicates regions of destabilization. Orange lines represent the cold-point tropopause height averaged over the 0-24-hour period. 30
- Fig. 6.** As in Fig. 5, but for the 24-48-hour period. 31
- Fig. 7.** As in Fig. 5, but for the 48-72-hour period. 32
- Fig. 8.** The contributions to the change in N^2 over the 24-48-hour period ($10^{-4} \text{ s}^{-2} (24 \text{ h})^{-1}$) by (a) horizontal advection and (b) vertical advection. (c) The radial velocity (m s^{-1} ; filled contours), potential temperature (K; thick black contours), cold-point tropopause height (orange line), and level of maximum outflow (dashed cyan line) averaged over the 24-48-hour period. (d) The vertical velocity (cm s^{-1} ; filled contours), potential temperature (K; thick black contours), and cold-point tropopause height (orange line) averaged over the 24-48-hour period. 33
- Fig. 9.** Ice mixing ratio (g kg^{-1}) and cold-point tropopause height (orange lines) averaged over (a) 0-24 hours, (c) 24-48 hours, and (e) 48-72 hours. Radiative heating rate (K h^{-1}) and cold-point tropopause height (orange lines) averaged over (b) 0-24 hours, (d) 24-48 hours, and (f) 48-72 hours. 35
- Fig. 10.** Schematic diagram of the effect of turbulent mixing on the vertical profile of potential temperature (θ). At the initial time (left panel), potential temperature is assumed to increase with height at a constant rate (thick black line). The imposition of turbulence within a portion of the layer (blue hatching) adjusts the potential temperature profile toward the mean

508	initial value of that layer. After a period of mixing (right panel) the potential temperature in	
509	the mixed layer does not vary with height, but just above and just below the mixed layer, it	
510	rapidly increases with height.	36
511	Fig. 11. Vertical eddy diffusivity ($\text{m}^2 \text{s}^{-2}$; filled contours), cold-point tropopause height (cyan lines),	
512	and radial velocity (m s^{-1} ; thick black lines) averaged over (a) 0-24 hours, (b) 24-48 hours,	
513	and (c) 48-72 hours.	37
514	Fig. 12. (Top panel) Change in N^2 over the 24-48-hour period ($10^{-4} \text{s}^{-2} (24 \text{ h})^{-1}$) directly output by	
515	the model for the 0-21-km layer. (Middle panel) Vertical eddy diffusivity ($\text{m}^2 \text{s}^{-2}$) averaged	
516	over the same time period. (Bottom panel) Radiative heating rate (K h^{-1}) averaged over the	
517	same time period.	39

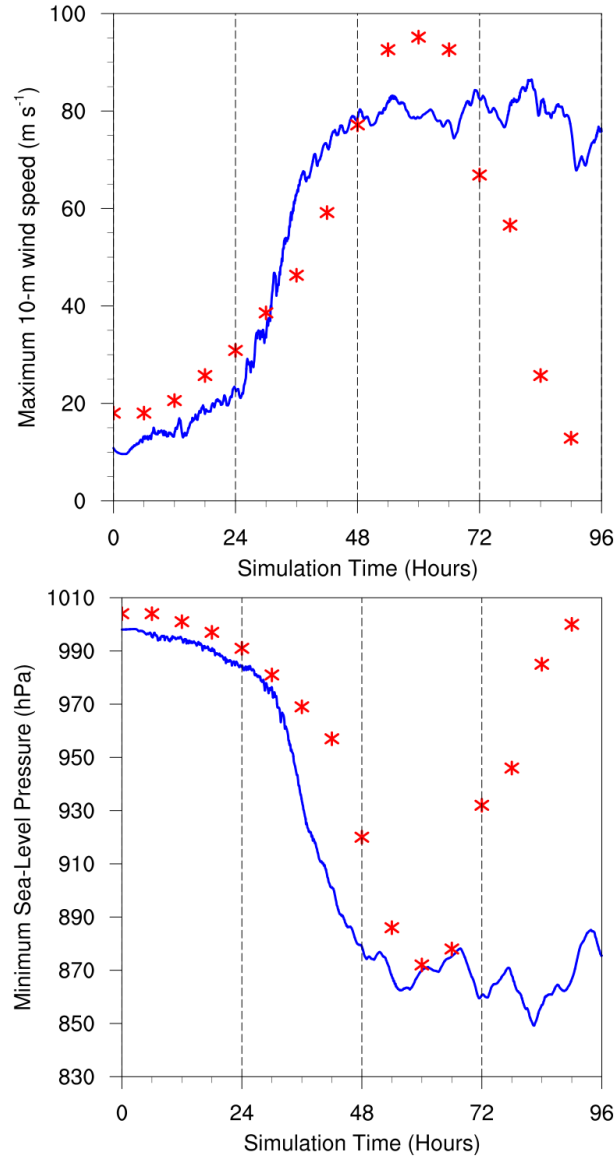


FIG. 1. The maximum 10-m wind speed (top panel; m s^{-1}) and minimum sea-level pressure (bottom panel; hPa) in the simulated storm (blue lines; plotted every minute) and from Hurricane Patricia's best track (red stars; plotted every six hours beginning at the time Patricia attained tropical storm intensity). The rapid weakening during the later stage of Patricia's lifetime was induced by landfall.

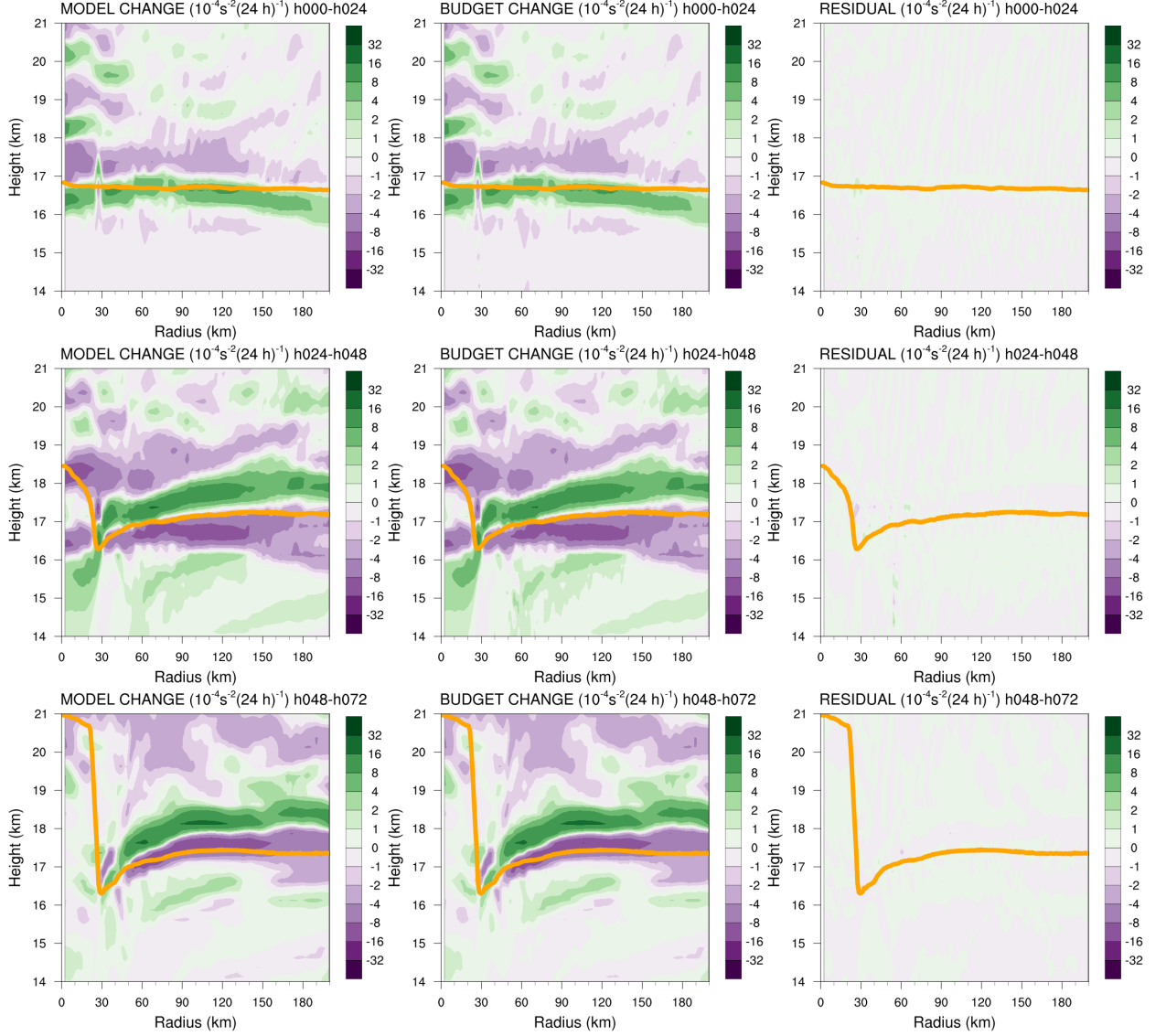


FIG. 2. Left panels: Twenty-four-hour changes in squared Brunt-Väisälä frequency (N^2 ; 10^{-4} s^{-2}) computed using Eq. 8 over (top row) 0-24 hours, (middle row) 24-48 hours, (bottom row) 48-72 hours. Middle Panels: The N^2 change over the same time periods computed using Eqs. 4-7, Right Panels: The budget residual over the same time periods, computed by subtracting the budget change (middle column) from the model change (left column). Orange lines represent the cold-point tropopause height averaged over the same time periods.

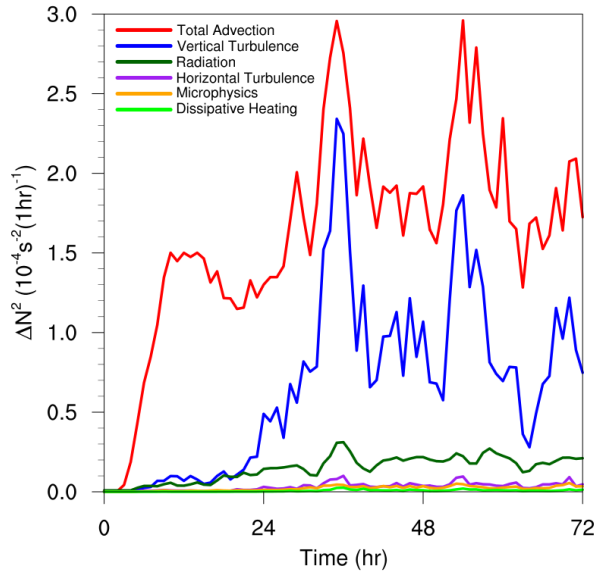


FIG. 3. Time series of the contribution of each of the budget terms to the time tendency of the squared Brunt-Väisälä frequency (N^2 ; 10^{-4} s^{-2}). For each budget term, the absolute value of the N^2 tendency is averaged temporally over 1-hour periods (using output every minute), and spatially in a region extending from 0 to 200 km radius and 14 to 21 km altitude.

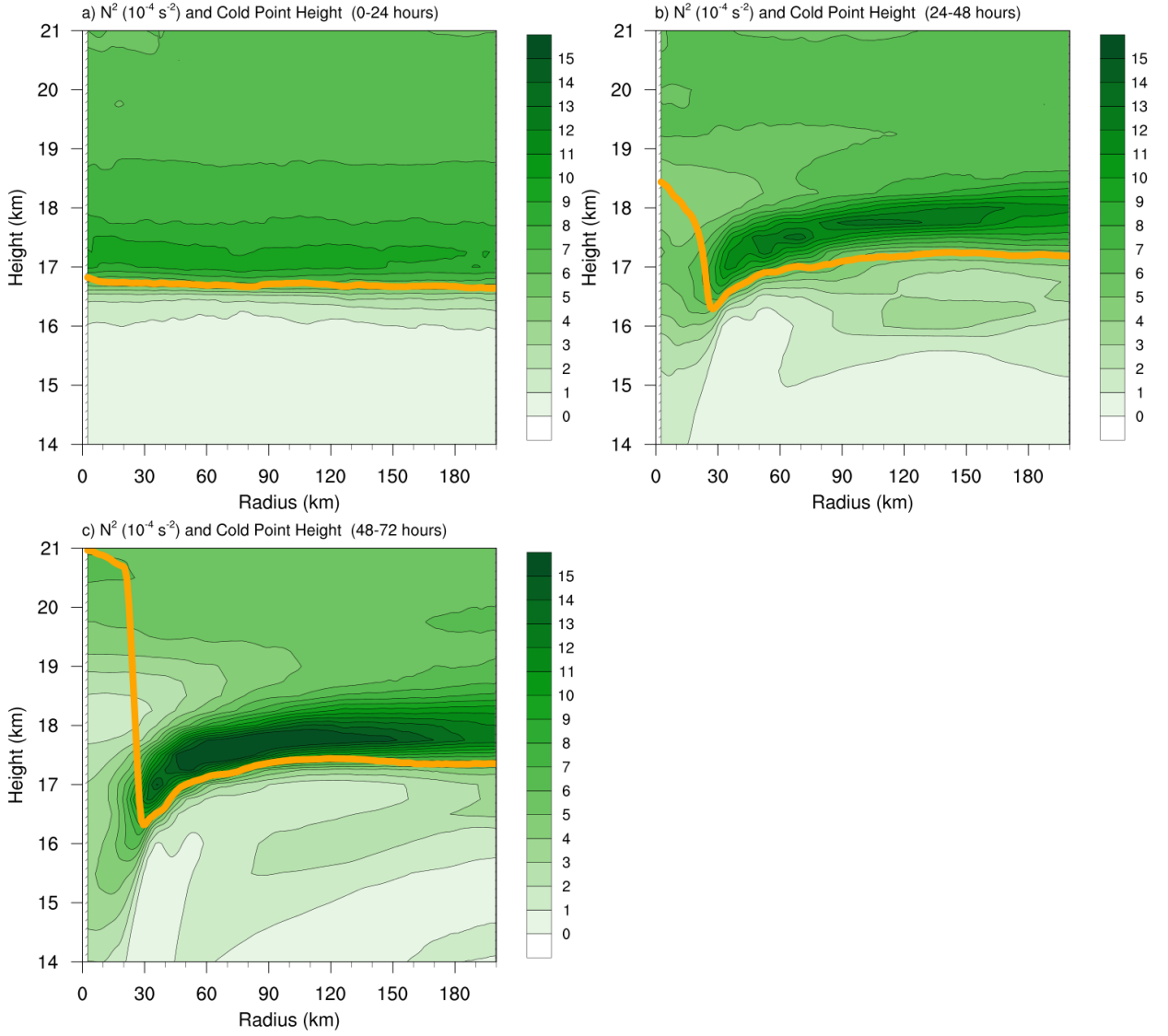
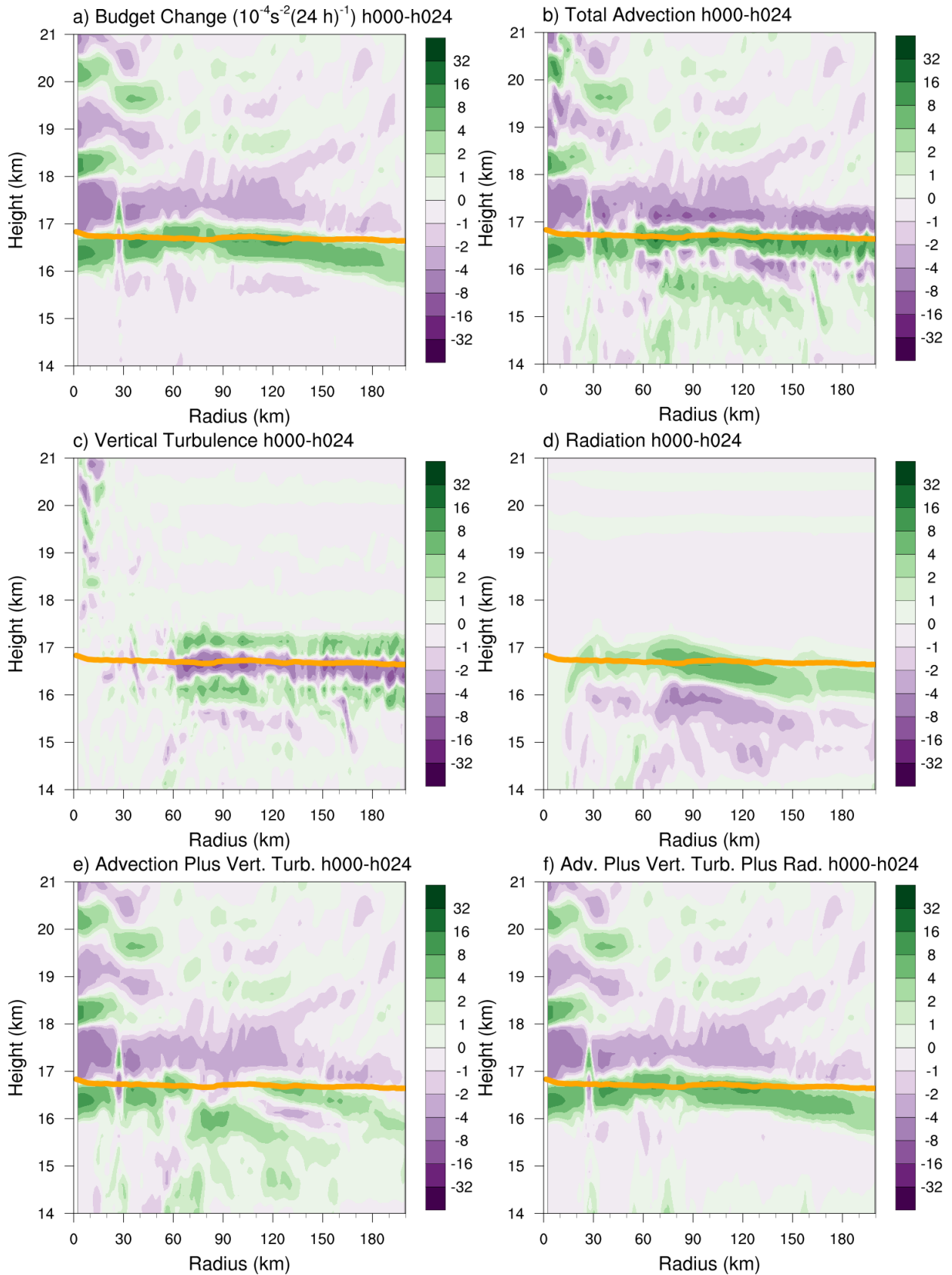


FIG. 4. Twenty-four-hour averages of squared Brunt-Väisälä frequency (N^2 ; 10^{-4} s^{-2}) over (a) 0-24 hours, (b) 24-48 hours, (c) 48-72 hours. Orange lines represent the cold-point tropopause height averaged over the same time periods.



534 FIG. 5. (a) Total change in N^2 over the 0-24-hour period ($10^{-4} \text{ s}^{-2} (24 \text{ h})^{-1}$) and the contributions to that change
 535 from (b) the sum of horizontal and vertical advection, (c) vertical turbulence, (d) longwave and shortwave
 536 radiation, (e) the sum of horizontal advection, vertical advection, and vertical turbulence, and (f) the sum of
 537 horizontal advection, vertical advection, vertical turbulence, and longwave and shortwave radiation. Green
 538 shading indicates regions of stabilization and purple shading indicates regions of destabilization. Orange lines
 539 represent the cold-point tropopause height averaged over the 0-24-hour period.

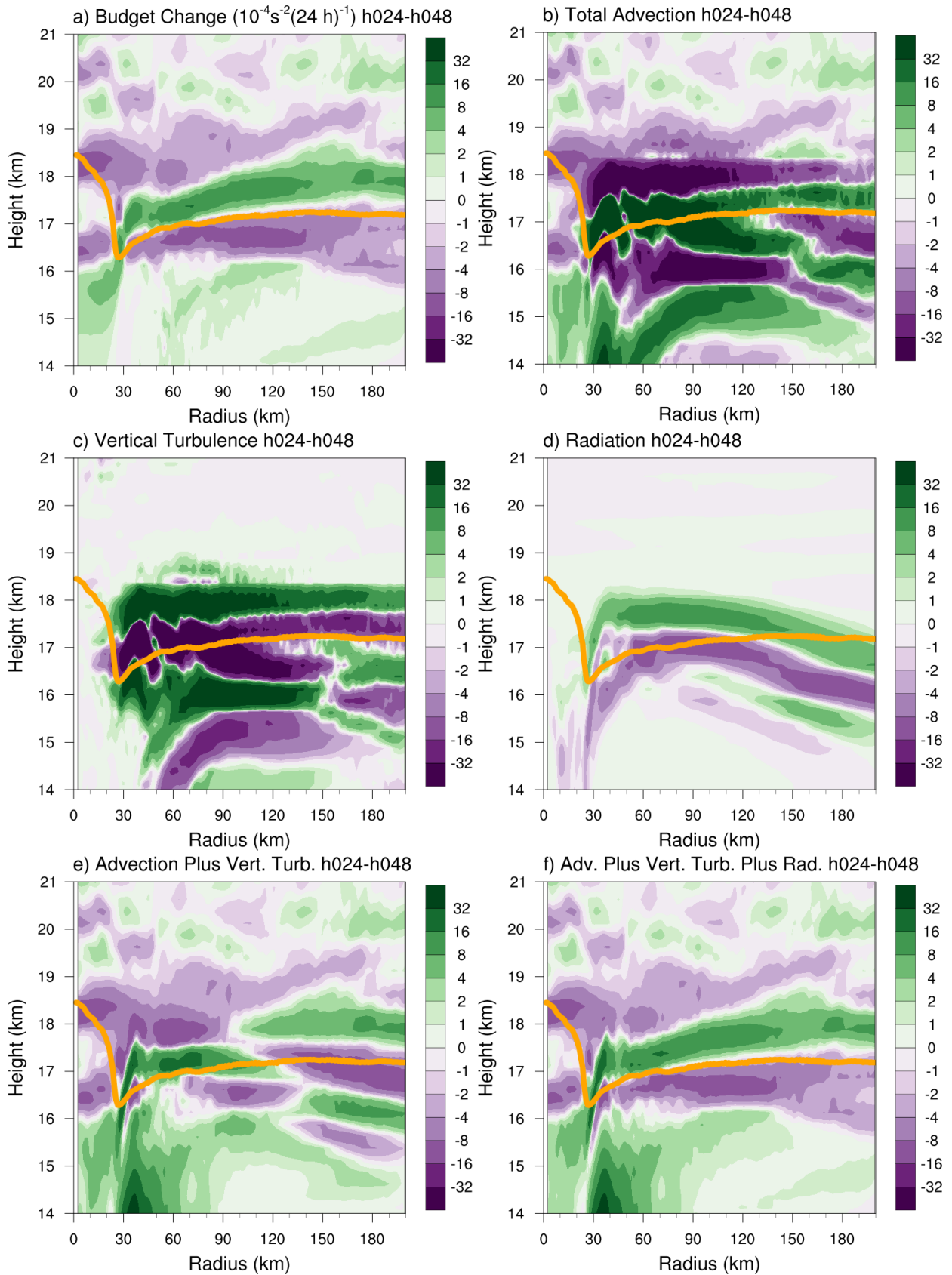


FIG. 6. As in Fig. 5, but for the 24-48-hour period.

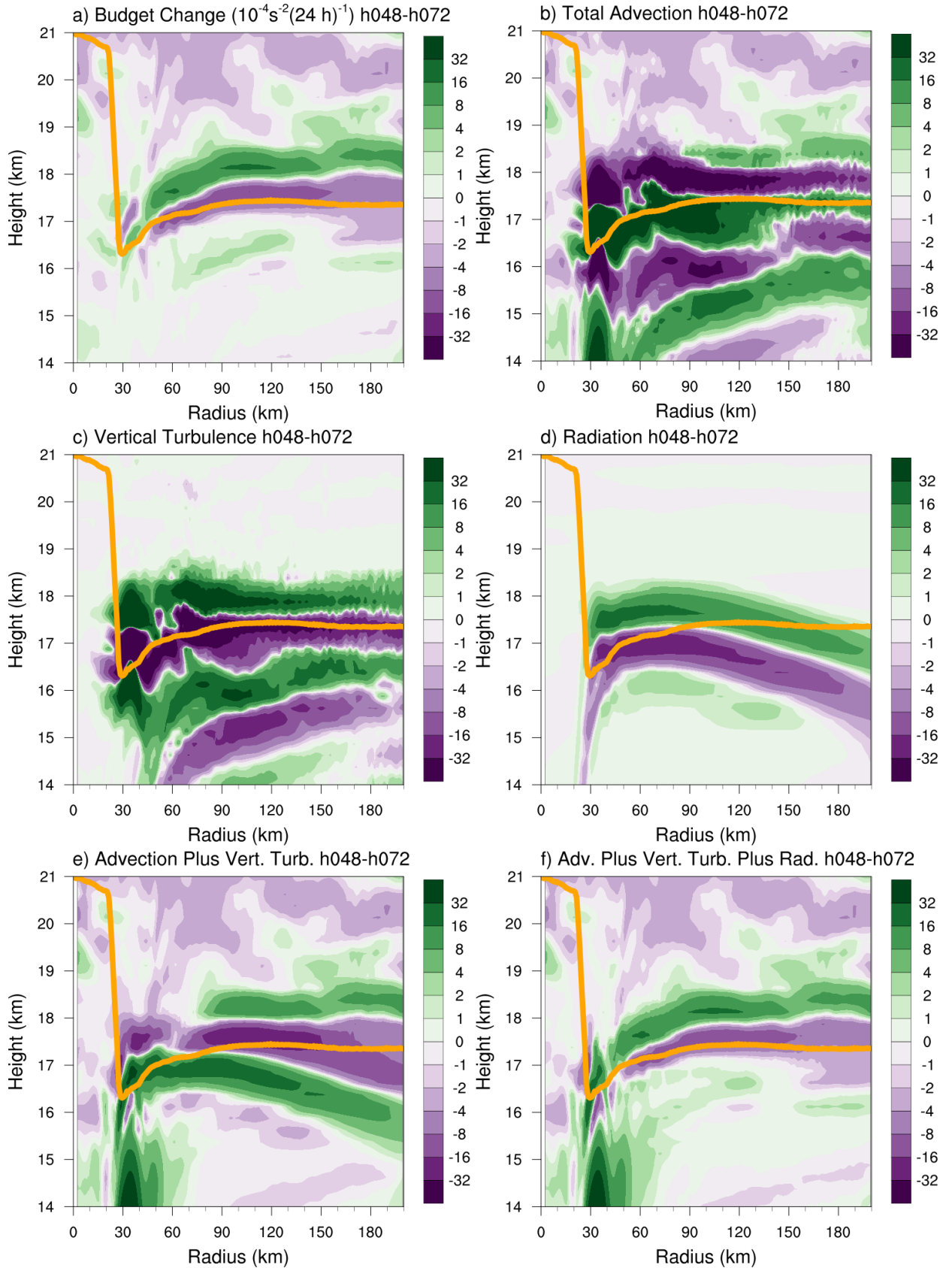


FIG. 7. As in Fig. 5, but for the 48-72-hour period.

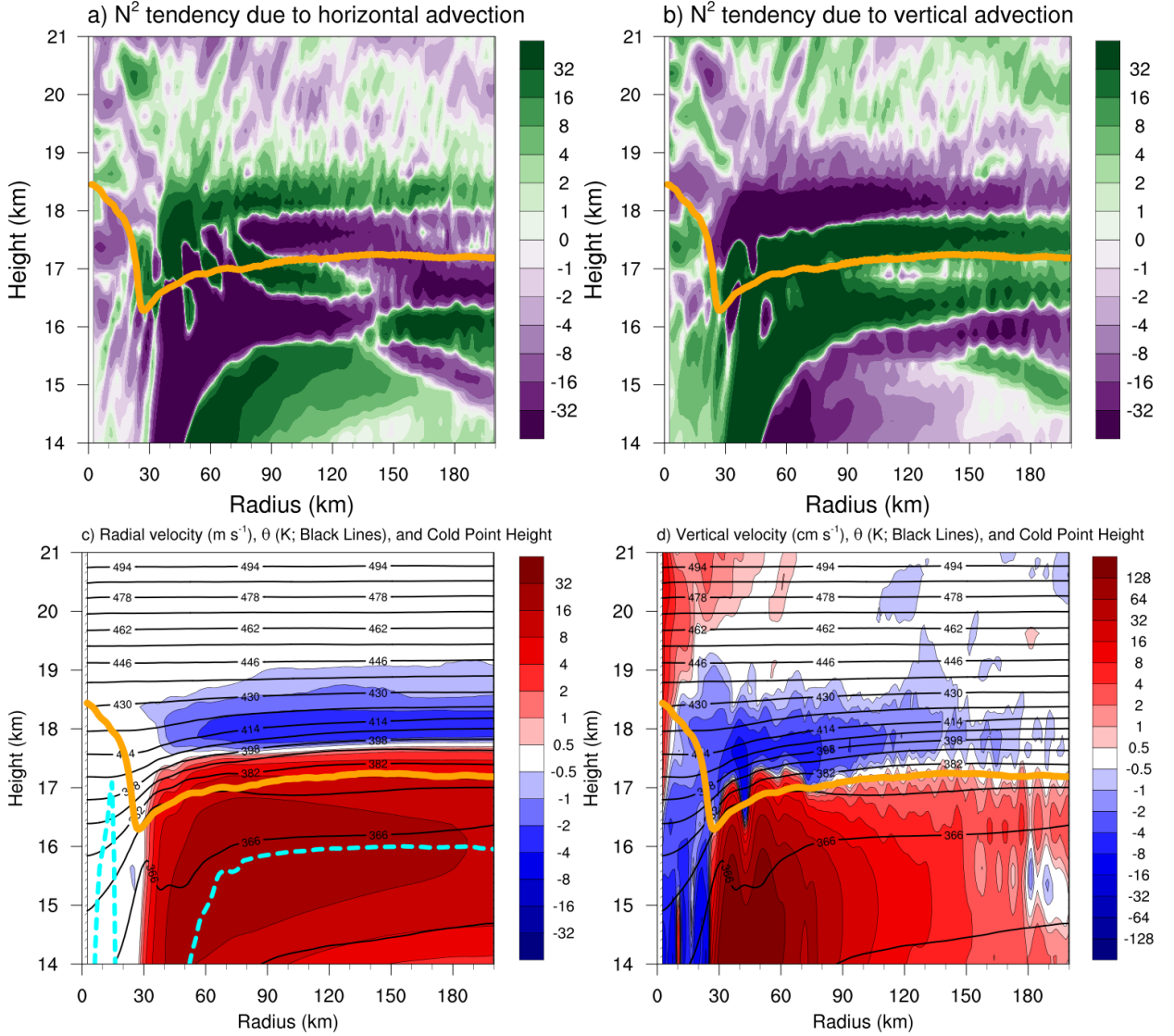
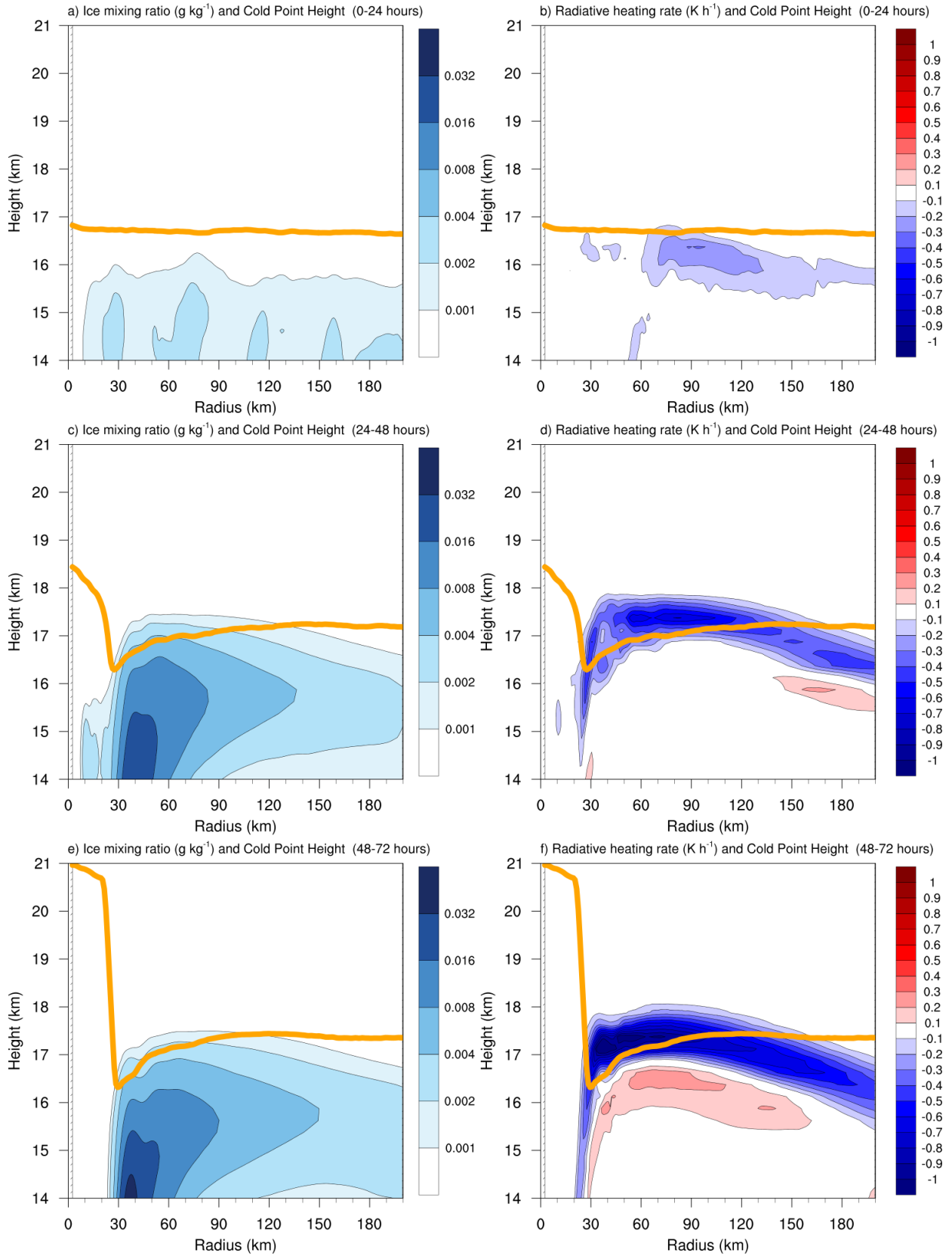


FIG. 8. The contributions to the change in N^2 over the 24-48-hour period ($10^{-4} \text{ s}^{-2} (24 \text{ h})^{-1}$) by (a) horizontal advection and (b) vertical advection. (c) The radial velocity (m s^{-1} ; filled contours), potential temperature (K; thick black contours), cold-point tropopause height (orange line), and level of maximum outflow (dashed cyan line) averaged over the 24-48-hour period. (d) The vertical velocity (cm s^{-1} ; filled contours), potential temperature (K; thick black contours), and cold-point tropopause height (orange line) averaged over the 24-48-hour period.



546 FIG. 9. Ice mixing ratio (g kg^{-1}) and cold-point tropopause height (orange lines) averaged over (a) 0-24 hours,
547 (c) 24-48 hours, and (e) 48-72 hours. Radiative heating rate (K h^{-1}) and cold-point tropopause height (orange
548 lines) averaged over (b) 0-24 hours, (d) 24-48 hours, and (f) 48-72 hours.

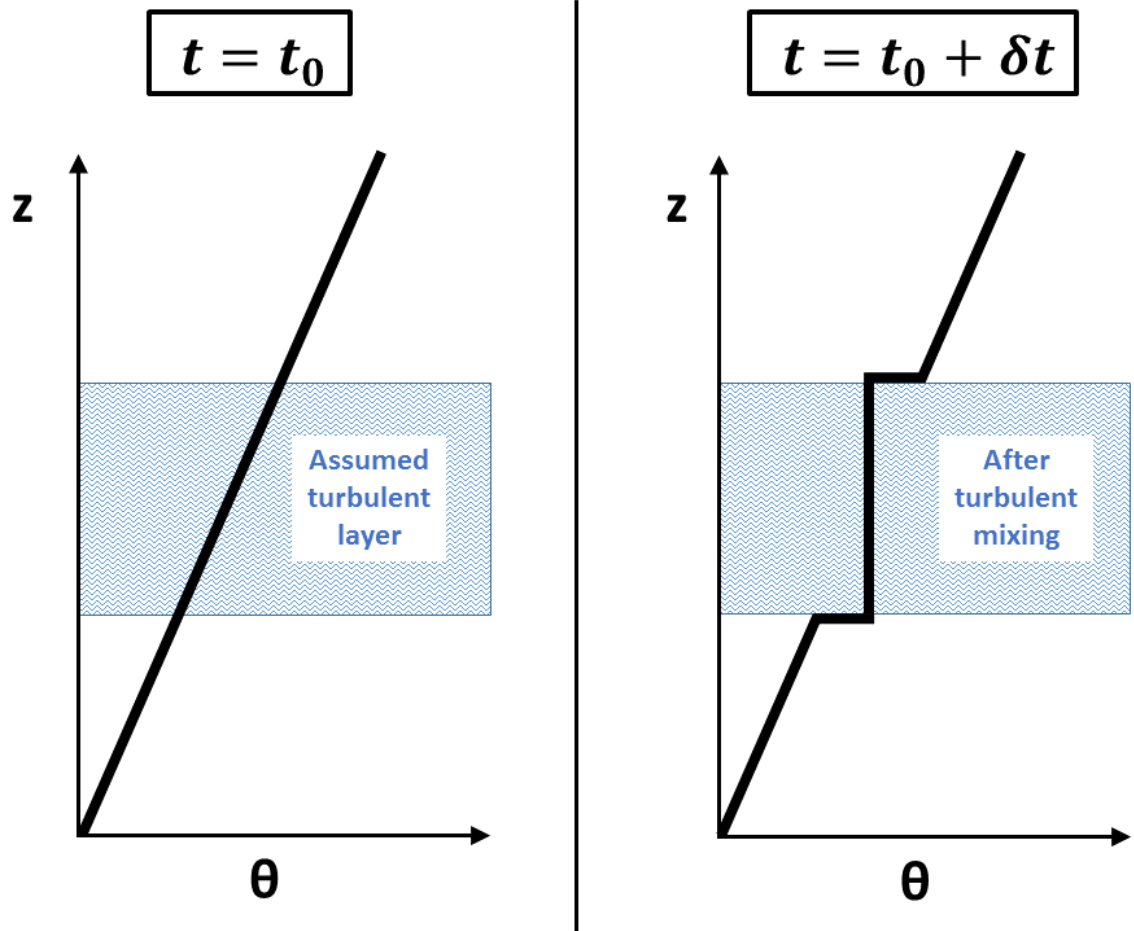


FIG. 10. Schematic diagram of the effect of turbulent mixing on the vertical profile of potential temperature (θ). At the initial time (left panel), potential temperature is assumed to increase with height at a constant rate (thick black line). The imposition of turbulence within a portion of the layer (blue hatching) adjusts the potential temperature profile toward the mean initial value of that layer. After a period of mixing (right panel) the potential temperature in the mixed layer does not vary with height, but just above and just below the mixed layer, it rapidly increases with height.

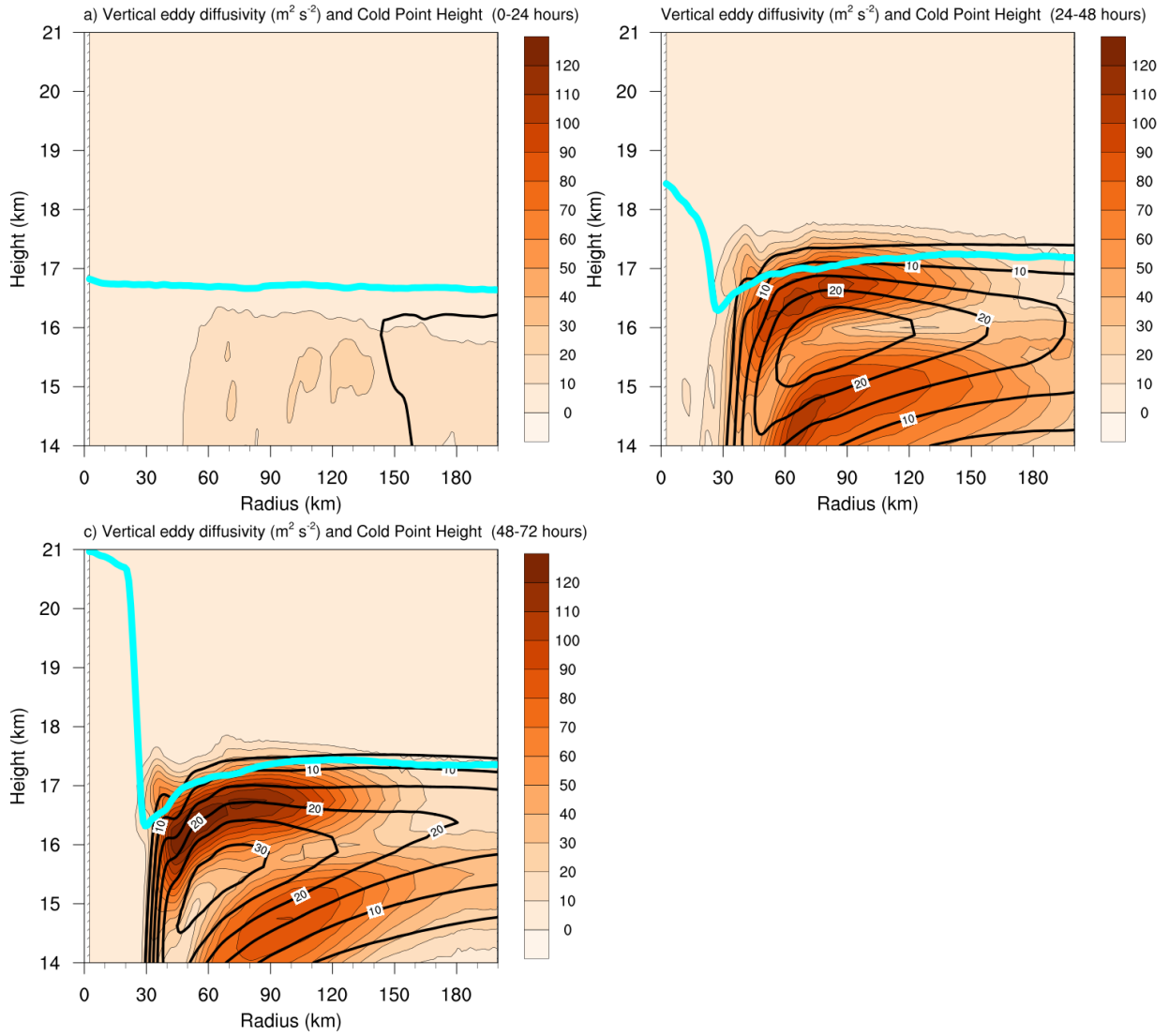
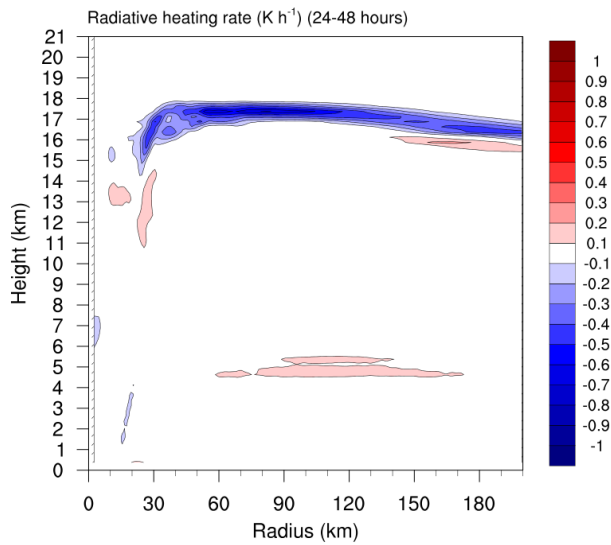
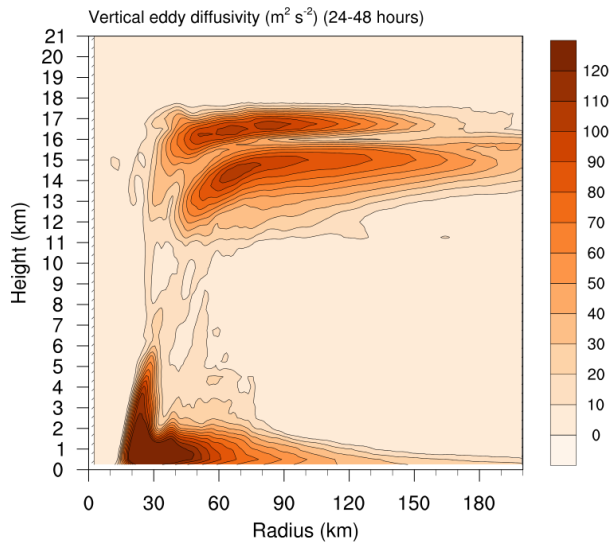
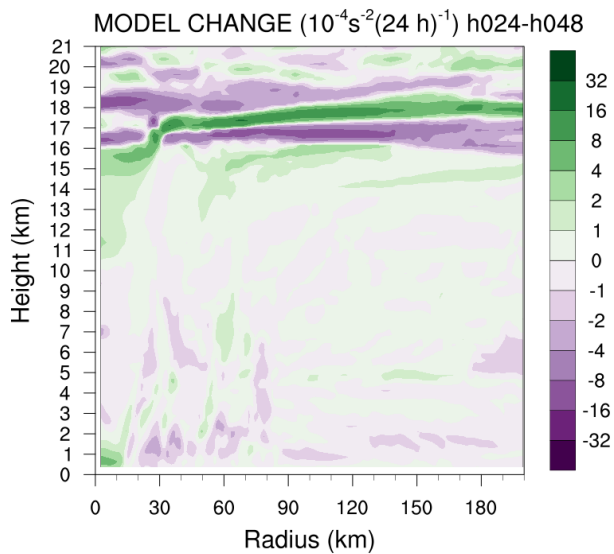


FIG. 11. Vertical eddy diffusivity ($\text{m}^2 \text{s}^{-2}$; filled contours), cold-point tropopause height (cyan lines), and radial velocity (m s^{-1} ; thick black lines) averaged over (a) 0-24 hours, (b) 24-48 hours, and (c) 48-72 hours.



557 FIG. 12. (Top panel) Change in N^2 over the 24-48-hour period ($10^{-4} \text{ s}^{-2} (24 \text{ h})^{-1}$) directly output by the model
558 for the 0-21-km layer. (Middle panel) Vertical eddy diffusivity ($\text{m}^2 \text{ s}^{-2}$) averaged over the same time period.
559 (Bottom panel) Radiative heating rate (K h^{-1}) averaged over the same time period.